Journal of Materials Processing Tech. 327 (2024) 118365

Contents lists available at ScienceDirect

Journal of Materials Processing Tech.

journal homepage: www.elsevier.com/locate/jmatprotec

Quick prediction of thinning in stretch forming of hat-shaped profiles during multi-stage hot sheet metal forming

Juri Martschin [a,*,1], Philipp Rethmann [a], Joshua Grodotzki [a], Malte Wrobel [b], Thomas Meurer [b], A. Erman Tekkaya [a]

[a] Institute of Forming Technology and Lightweight Components, Baroper Straße 303, Dortmund 44227, Germany
[b] Digital Process Engineering - Institute of Mechanical Process Engineering and Mechanics, Hertzstr. 16, Karlsruhe 76187, Germany

ARTICLE INFO

Keywords:
Stretch forming
Progressive die
Control
Closed-loop
Hot stamping
Press hardening

ABSTRACT

A novel quick model predicting the thinning distribution in hot stretch forming of hat-shaped profiles as a building block for a closed-loop control of a multi-stage forming process operated at a stroke rate of up to 12 strokes/min (5 s per stroke) is presented. The key characteristic of this new model is that it considers both a spatially as well as time-variant temperature distribution within the blank during forming. This is achieved by using temperature sensors and applying the information as input for the model, which is based on force equilibria and the theory of plasticity. The model predicts the geometry of the formed part which can be used as crucial input information to the process control. For the quick model, an element-based time-discrete approach was chosen. By assuming a plane strain condition and a decoupling of thermal and mechanical computation as well as by adapting further assumptions, the calculation time on a current desktop PC is 4 s. The achieved calculation time is sufficiently short to realize the control at the given stroke rates. The model is validated by experiments using a hot stretch forming setup designed to simulate the multi-stage process. The model successfully replicates the influence of various stroke rates on the final thinning distribution and predicts the effects of diverse pre-cooling scenarios.

1. Introduction

In hot sheet metal forming, the temperature distribution in the blank both before and during forming is decisive for the resulting thinning distribution in the parts produced. Warmer sheet metal areas exhibit a lower yield stress compared to colder sheet areas, resulting in strain localization and therefore increased thinning within the warmer areas. Maeno et al. (2014) demonstrated in the hot stamping of cups, that the temperature and therefore the sheet thinning distribution can be influenced by varying the punch speed and hereby the heat exchange of the blank with the die. Suzuki et al. (2018) altered the thinning distribution in die bending of w-shaped parts by adjusting the temperature distribution via the contact pressure of the gripper for transporting the sheet metal from the furnace to the bending-die. Another approach used to set the thinning distribution in hot sheet metal forming is the cooling of selected sheet metal areas with compressed air before and during the forming operation within the stamping die (Ota et al., 2014).

The methods and actuators mentioned above were all applied to single-stage hot sheet metal forming processes. Multi-stage hot sheet metal forming processes, implemented in a transfer or progressive die, offer the potential to adjust the temperature distribution in the sheet, not just once but also step by step. This can be achieved using cooling or heating stages with localized temperature control features, as well as other actuators integrated into the die system. In multi-stage press hardening of Zn-coated steel in a transfer die, an initial cooling stage lowers the temperature prior to the forming stages, while the actual dies are heated to control the temperature drop within the forming stages (Belanger et al., 2017). Also, concepts for inductive heating (Löbbe et al., 2015), DC-heating (Mori et al., 2017) as well as re-austenitization (Demazel et al., 2018) within progressive dies have been developed, allowing flexibly adjusted temperature before forming.

With the degrees of freedom for adjusting the thermal history within the die system, multi-stage hot forming supplemented by a closed-loop property control provides the opportunity to set the sheet thinning by

* Corresponding author.
E-mail addresses: office@iul.tu-dortmund.de, Juri.Martschin@iul.tu-dortmund.de (J. Martschin), verwaltung@mvm.kit.edu (M. Wrobel).
[1] https://orcid.org/0000-0002-4213-3739

https://doi.org/10.1016/j.jmatprotec.2024.118365
Received 30 October 2023; Received in revised form 1 February 2024; Accepted 4 March 2024
Available online 6 March 2024

means of controlling the temperature distribution within the blank. Thus, parts with tailored properties can be produced in small batch sizes while minimizing the number of scrap parts. However, to achieve this, control-oriented, i.e., quick models are an essential requirement, allowing to feed the product properties back within a control loop and to derive the actuator settings for the property control. Such models, which calculate the sheet metal thinning online during the process in a sufficient time span, with the requirement to take into account a non-uniform as well as time-varying temperature distribution, are not yet available. Tricarico and Palmieri (2023) presented a model for the process of deep drawing based on numerical simulations, that is applicable for in-line control of the draw-in and hereby the sheet thinning. However, this model only works for forming at room temperature, wherefore hot sheet metal forming processes are out of scope. Accounting for temperature, Attar et al. (2021) introduced a convolutional neural network for the determination of the local thinning in hot forming, which performs sufficiently fast to be used in process control. However, the network only accounts for temperature distributions which are initially homogeneous. Such a state is rarely observed in complex multi-stage forming. Additionally, the network-based model only performs well within the boundaries of the initial training data. This greatly limits the applicability of the model regarding a robust use within closed-loop control accounting for a wide range of process conditions.

As a result, the goal of this work is to develop a physical process model, which predicts thinning sufficiently fast to be used in closed-loop controlled multi-stage hot sheet metal forming processes. Crucially, it is required that the model accounts for spatially and time-varying temperature distributions within the blank, as such conditions are frequently found in complex hot forming processes. The model acts as the basis for the control engineering of the forming process, which is to be realized in future works. As a reference case, which exhibits similar conditions as actual processes, a simplified hot stretch forming process of hat-shaped profiles in a progressive die is chosen. In the following, the process and the control concept (i.e. the framework) are presented. Next, a test setup serving for carrying out model validation hot stretch forming experiments is described. Subsequently, a model for the control-oriented prediction of sheet thinning in hot stretch forming of hat-shaped profiles is derived and validated on the basis of a comparison between model and experimental data.

2. Closed-loop controlled hot stretch forming in multi-stage hot sheet metal forming

To define the scope of this investigation, hot stretch forming of sheet metal is assumed to be part of closed-loop controlled multi-stage hot sheet metal forming for the production of hardened hat-shaped profiles (Fig. 1). The heating, forming and quenching stages are implemented in

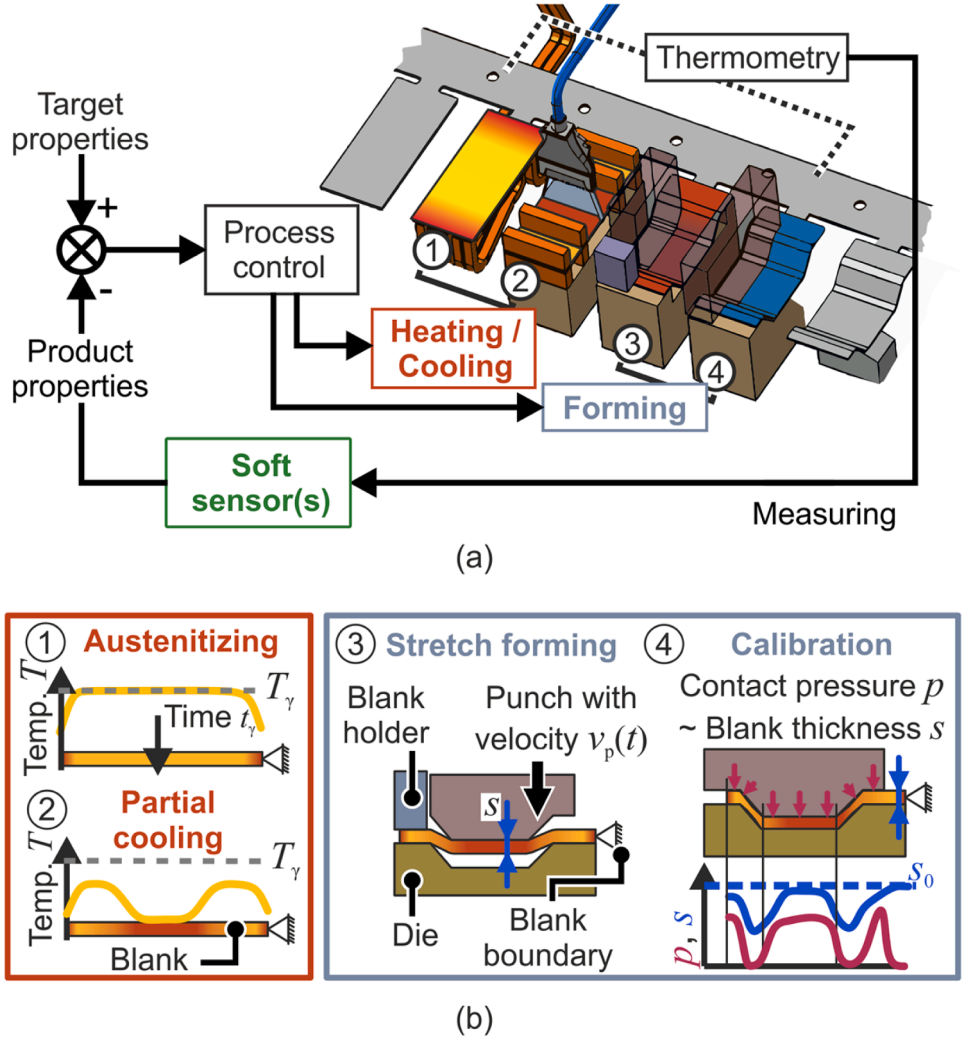

Fig. 1. Multi-stage hot sheet metal forming process. (a) Process design for multi-stage hot sheet metal forming with a closed-loop control of product properties in a progressive die. (b) Principle of the heating, cooling and forming stages of the process setup.

a progressive die, which is mounted to a servo press. Following the pre-punching stages, the sheet is rapidly heated to the austenitization temperature T_γ by induction heating (1) and is held at this temperature for the duration of the dwell time t_γ. The austenitization parameters (T_γ, t_γ) represent adjustable control variables for setting the hardness and for pre-controlling the initial sheet temperature in the subsequent forming stages (Löbbe et al., 2016). After austenitizing, the sheet can be partially cooled (2) with compressed air to pre-set the flow of the material in the subsequent stages by setting a specific temperature profile resulting in locally varying temperature dependent flow stresses (Ota et al., 2014). The control variables within the second stage for setting a targeted temperature profile are the duration of the forced air cooling t_c and, optionally, the volumetric flow rate. In the third stage, the sheet is stretch formed (3) to the hat-shaped profile, whereby the sheet thinning Δs, which is the focus of this work, is set. For this stage, the kinematics of the tools, which here is specified by the punch speed v_p as a function of time t, represents an additional control variable. Varying tool kinematics result in different contact times of the tool elements with the sheet metal blank and thus a locally varying cooling and flow of the material during forming (Maeno et al., 2014). In the calibration stage (4), the hat-shaped profile is calibrated as well as quenched.

For setting the sheet thinning as well as the hardness online and for a simultaneous compensation of the process uncertainties, the setup is supplemented by a closed-loop control. For this purpose, sheet thinning must be measured and fed back online. However, direct measurement of the thinning distribution is not possible due to the limited space available and the rough environment (electromagnetic field, high temperature). Therefore, a concept similar to that of a soft sensor (Kadlec et al., 2009) is realized. First, during the multi-stage process, the sheet temperature is recorded locally at selected measuring points throughout all tool stages, e.g. using thermocouples, pyrometers, or thermal imaging cameras. At the same time, the temperature distribution in the sheet metal is reconstructed from these measurement data using a temperature estimator according to Kloeser et al. (2021) or Martschin et al. (2023). Based on the temperature estimation, the control-oriented, i.e. quick, model developed in this paper will then predict the thinning during stretch drawing with an element-based approach. The output of the model is then compared with the target properties (i.e. the thinning distribution) and, based on this, the above-mentioned control variables (austenitization parameters, duration and volumetric flow rate of the forced air cooling, punch speed) must be modified.

3. Material

The experimental investigations in this paper are carried out with the martensitic stainless steel X46Cr13, which is in the form of sheets with a thickness of 2 mm (see as-received condition in Table 1). The quenched hardness of this air-hardening steel has a low sensitivity towards the cooling rate. A martensitic microstructure with a hardness of 700 HV10 can be set even when cooling at rates of 3 K/s after the austenitization (Behrens et al., 2018). Therefore, the variation of the cooling rate in the process presented above by air cooling only has a negligible impact on the post-forming properties of this steel. The suitability of such air-hardening capabilities for multi-stage press hardening is demonstrated by Hamamoto et al. (2017). In addition, the hardness of X46Cr13 sheet material can be tailored by controlling the austenitization temperature and dwell time during rapid austenitization (Martschin et al., 2021). In terms of designing a multi-stage hot sheet metal forming process, it is also advantageous that the low martensite start temperature of ~170 °C (Dieck et al., 2017) provides a sufficiently wide process window for carrying out several forming operations after the austenitization.

For the modeling of the sheet thinning distribution in the stretch forming stage of the assumed multi-stage process, a temperature-dependent description of the elastic and plastic material behavior of the X46Cr13 sheet material is required. The experimental characterization of these properties is described in the following sections.

3.1. Temperature dependent flow stress

The flow stress is intrinsically linked to the microstructure, which in turn depends on the thermo-mechanical history. Hot tensile tests are carried out that simulate the thermo-mechanical history of the real process. The hot tensile setup (Fig. 2**a**) is analogous to Löbbe et al. (2016) implemented on a universal testing machine (Z250, Zwick Roell).

First, the gauge length region of the tensile test specimen is inductively heated to the austenitization temperature $T_\gamma = 1100$ °C in a time span of 10 s. This temperature is maintained for the dwell time $t_\gamma = 5$ s. For heating an induction generator (AXIO 10/450 HF, TRUMPF Hüttinger) is used. In the next step, the specimen is cooled to the forming temperature T_ε with the cooling rate $r_c = 30$ K/s. Fast cooling is realized by two multi-channel flat fan nozzles (600.493.1Y.AC., Lechler). The pressurized air supply of these nozzles is switched on immediately after the dwell time. To avoid bending of the specimen due to thermal expansion during heating and cooling, the specimen is pre-loaded during these phases with a force of 50 N, which produces a negligible stress of 2 MPa in the tensile direction in the gauge length region. Finally, the hot tensile test is performed at a constant temperature (isothermal). Concurrently, a tactile measuring device (PMA-12/V7–1, Maytec) records the elongation of the gauge length region over time $\Delta l(t)$. The T-t-curve of the described near-process tensile-test (Fig. 2b) is set by a PID-controller (Regulus RD, SensorTherm) adjusting the power of the induction generator based on the feedback from two pyrometers, which are focused on the center of the specimen. For improved accuracy, the temperature range 150 °C $< T <$ 600 °C is measured with the first pyrometer (Metis M318, SensorTherm) and the temperature range 600 °C $< T <$ 1400 °C is measured with the second pyrometer (Metis M308, SensorTherm). In addition, to verify a sufficient temperature distribution in the forming zone, a thermal imaging camera (TIM-M1, Micro-Epsilon) is also pointed at the sample. During experiments, a temperature deviation of ± 7 °C over the gauge length region and the specimen width was observed.

An extract from the obtained flow curves is given in Fig. 3. To handle the flow curves within the stretch forming model to be developed, as well as their extrapolation for true strains $\varepsilon_\Phi > 0.1$, an extended Norton-Hoff approach (Brosius et al., 2007) is fitted:

$$k_f = K \bullet (b + \varepsilon_\Phi)^{n_0 \bullet \exp(-c_n \bullet (T - T_0))} \bullet \dot{\varepsilon}^{m_0 \bullet \exp(-c_m \bullet (T - T_0))} \bullet \exp(\beta / T) \quad (1)$$

Improved accuracy is achieved by fitting the parameters β, n_0 and m_0 of the flow curve approximation dependent on the forming temperature T_ε (Table 2). The parameters K, b, c_n, c_m and T_0 are kept constant. The results of the fitting (Mod.) are plotted in Fig. 3. Fitting the modified Johnson-Cook model from Cowper and Symonds (1957) and the Nemat-Nasser (2002) model results in larger mean square errors compared to the above described fitting of the extended Norton-Hoff model, and

Table 1
As-received condition of the X46Cr13. Yield Strength, hardness and chemical composition according to the mill certificate in conformity with EN 10204/3.1.

Yield Strength $R_{p0.2}$ in MPa	Hardness in HV	Chemical Composition in wt%						
		C	Si	Mn	P	S	Cr	Fe
372	245	0.443	0.37	0.55	0.026	0.001	13.76	84.85

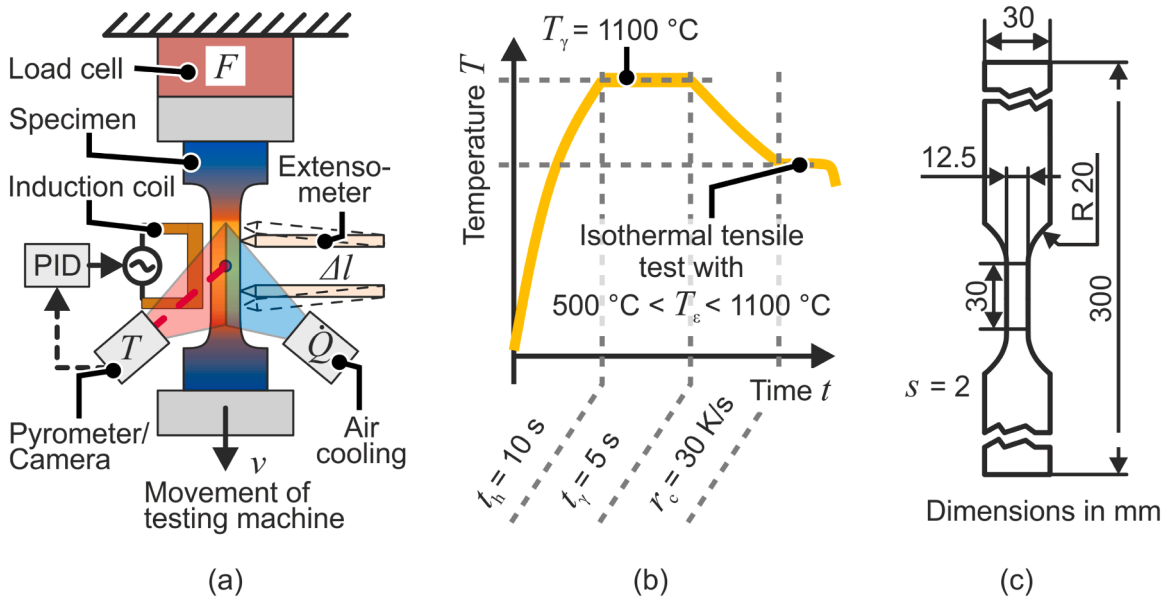

Fig. 2. Near-process tensile tests. (a) Setup for the near-process tensile tests. (b) Parameters of the time-temperature curve for the near-process tensile test. (c) Geometry of the tensile test specimen with units in mm.

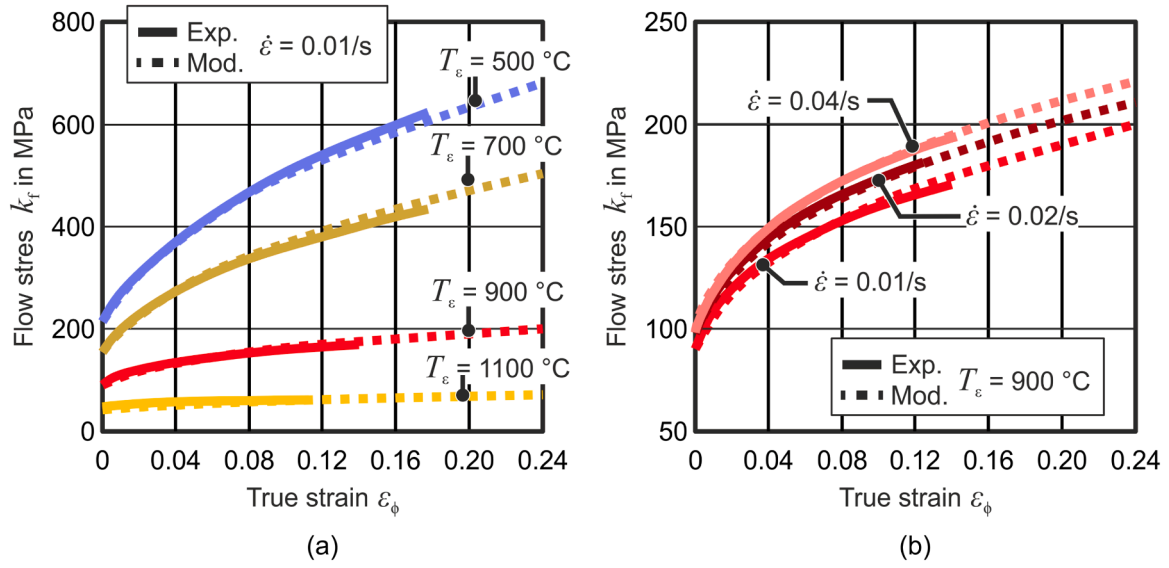

Fig. 3. Flow curves of X46Cr13. Examples of measured flow curves from the experiments (Exp.) and plots of the flow curve extrapolation on the basis of the flow curve model (Mod.) for the X46Cr13 sheet material. (a) Variation of the forming temperature at constant strain rate. (b) Variation of the strain rate at constant forming temperature.

Table 2
Identified parameters for the Norton-Hoff model. Constant and variable fitting parameters dependent on the forming temperature.

Constant fitting parameter						
K	***b***	c_n		c_m	T_0	
156.94	0.011	9.50E-5		5.98E-4	1100 °C	
Variable parameter	**Forming temperature T_ε in °C**					
	500	**600**	**700**	**800**	**900**	**1000**	**1100**
β	987.40	1157.91	1194.84	1079.60	807.44	472.22	16.09
n_0	0.35	0.38	0.36	0.29	0.24	0.20	0.15
m_0	5.00E-4	5.00E-4	5.80E-3	3.49E-2	6.03E-2	9.27E-2	1.21E-1

therefore, is not used in this investigation.

3.2. Temperature dependent Young's modulus

To account for measurement uncertainties (Lord and Morrell, 2010) and temperature related effects (Pérez Caro et al., 2021), the Young's modulus during hot forming has to be determined as an average value from several consecutive loading and unloading cycles during the tensile test. In the frame of this investigation, those cyclic loading-unloading tensile tests are carried out with the same experimental setup and step sequence as described above (compare Fig. 2b). However, instead of drawing the tensile test specimen once after austenitization and cooling, three loading-unloading cycles are performed, each with 2% strain. Since a pronounced influence of the strain rate on the Young's modulus during hot forming is not known, the tests are carried out under quasi-static conditions with a strain rate $\dot{\varepsilon}$ of 0.001. From the data obtained, an average Young's modulus is calculated (Fig. 4).

4. Hot stretch forming

4.1. Experimental setup

In order to experimentally determine the thinning Δs that is set during hot stretch forming with respect to different temperature distributions and stroke rates, forming experiments are performed with a setup that simulates the step sequence of the before presented multi-stage hot sheet metal forming process (Fig. 5). The tooling system is operated in a servo press (MSD2–400, Schuler) to replicate the kinematics, i.e. the ram speed profile, of the multi-stage process. First, the austenitization stage (stage 1) is simulated. A sheet metal strip from X46Cr13 with a length of 200 mm, a width of 38 mm and a thickness of 2 mm is clamped between current terminals for a length of 20 mm on each outer side. The current terminals are connected to a DC generator that provides a maximum output power of 40 kW at a current of 2000 A and a voltage of 20 V. By resistance heating, the strip is heated to the austenitization temperature $T_\gamma = 1100$ °C with a rate $r_h = 110$ K/s. This temperature is held for a dwell time t_γ of 5 s in order to ensure a homogeneous temperature distribution over the specimen's length and width.

The temperature-time-profile is set by a PID-controller (Regulus RD, SensorTherm) which adjusts the power of the DC generator based on the feedback from a pyrometer (Metis M308, SensorTherm), which measures the current temperature at the strip center. After the dwell time of the austenitization phase, the pre-cooling stage of the multi-stage press hardening process is simulated (stage 2). To modulate the temperature profile over the length of the specimen, two multi-channel flat fan nozzles (600.493.1Y.AC., Lechler) are used, which allow the setting of a spatially limited cooling due to their laminar airflow (Fig. 5b). The nozzles are connected to a compressed air network (average pressure 8 bar) via a pressure reducer and are operated at 5 bar. A controllable

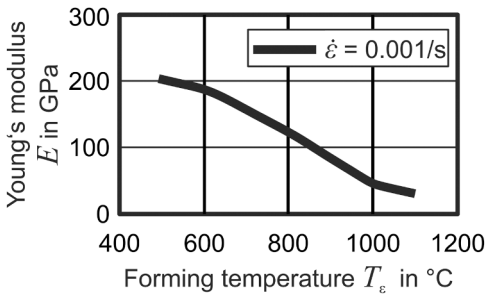

Fig. 4. Temperature dependence of the Young's modulus of X46Cr13. Young's modulus averaged from several consecutive isothermal loading and unloading cycles.

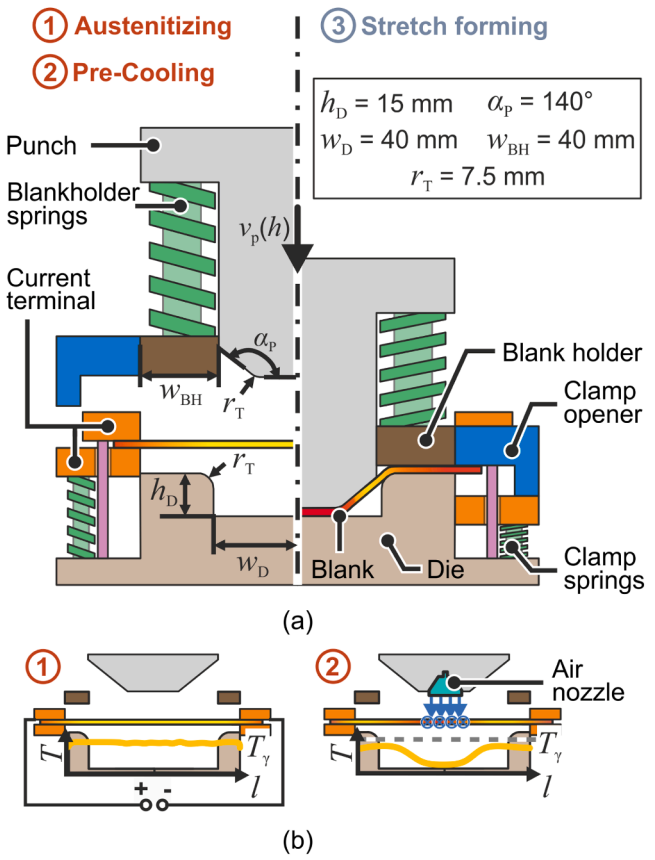

Fig. 5. Experimental setup for hot stretch forming with pre-cooling. (a) Setup and steps 1–3 for hot stretch forming. (b) Temperature distribution after austenitization and pre-cooling with compressed air from an air nozzle.

solenoid valve (VPPM, Festo) is used to switch the compressed air on and off. The specimen is exposed to a lateral air stream from each of the air nozzles for the pre-cooling time $t_c = 5$ s. By indicating the nozzle in the 2D illustrations in this work, the aim is solely to show their position and effect along the longitudinal coordinate l. The pressurized air is not directed onto the metal strip from below or above but laterally. The resulting temperature distribution across the specimen width was measured with a thermal imaging camera (TIM-M1, Micro-Epsilon) directly after pre-cooling. The maximum observed temperature difference was around 20 K. Therefore, in the following, the temperature gradient in the width direction is neglected. With the described setup

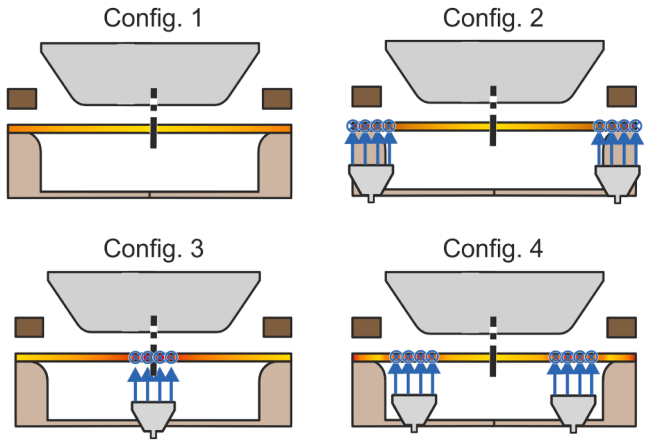

Fig. 6. Pre-cooling configurations. Configurations (Config.) for setting different temperature distributions before stretch forming.

four different pre-cooling configurations (short: config.) are considered, which can be set before the forming operation (Fig. 6):

•Configuration 1: No active pre-cooling (ambient cooling) and direct start of press movement.

•Configuration 2: Pre-cooling of the flanges of the hat-shaped profile.

•Configuration 3: Pre-cooling of the bottom of the hat-shaped profile.

•Configuration 4: Pre-cooling of the side walls of the hat-shaped profile.

Temperature distributions set by pre-cooling that are not symmetrical with respect to the longitudinal direction of the specimen are not considered.

The last test step of the investigated procedure is the stretch forming (step 3). Directly after pre-cooling, the forming operation is conducted. During the downward movement of the upper tool, the clamp opener first opens the current terminals. This releases the sheet and allows longitudinal thermal expansion caused by the austenitization step to be compensated. Afterwards, a pre-tensioned blank holder fixes the sheet metal strip and the punch forms the hat-shaped profile. Upon reaching the bottom dead center, the punch remains at that position until the end of the stroke, which is also the end of each experiment, at which point the sheet metal strip is quenched in the closed tool. To implement the above-mentioned sequence, the servo press is operated in a single-stroke mode.

The punch speed v_p is a function of the drawing depth h and varies with the set stroke rate f_{SR} of the used servo press (Fig. 7). As a result of the specific punch and die geometry, the majority of the deformation, around 50% of the idealized sheet stretching ε_Φ, is induced during the final 30% of the stroke (10 mm $< h <$ 15 mm). At the beginning of the lower third of the stroke ($h = 10$), the punch speed v_p is already reduced to half of the initial speed.

4.2. Measurement of the temperature distribution

During forming, the temperature distribution of the sheet metal strip is measured with a thermal imaging camera (TIM-M1, Micro-Epsilon) at a frame rate of 80 Hz. A distance of ~300 mm is maintained between the thermal imaging camera and the outer edge of the clamped specimen. This results in a resolution of 14 pixels for the sheet thickness. Before forming, the outer edges of the sheet metal strip are polished to remove the burr and thus improve the quality of the temperature measurement. The implemented setup for the config. 3 and an example for the temperature distribution measured with the thermal imaging camera are given in Fig. 8.

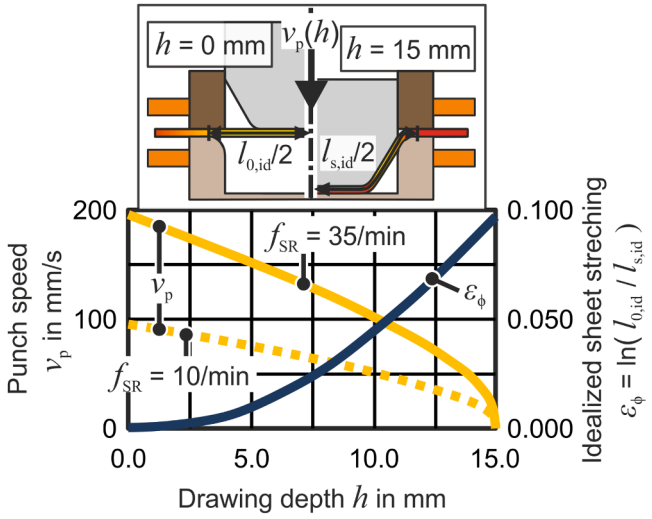

Fig. 7. Dependencies of the punch speed and thinning. Punch speed v_p with a stroke rate f_{SR} of 10 and 35 strokes per minute and idealized sheet stretching ε_Φ depending on the drawing depth h.

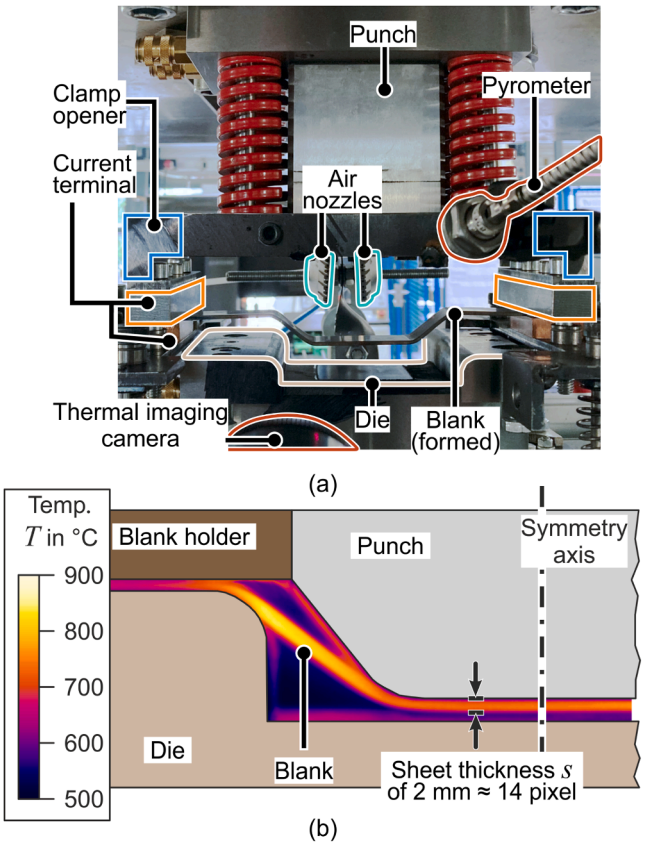

Fig. 8. Implementation of the test setup. (a) Alignment of the thermal imaging camera and the air nozzles (according to configuration 3). (b) Temperature distribution obtained with the thermal imaging camera at a drawing depth h = 14 mm.

4.3. Measurement of the thickness distribution after forming

The sheet thickness is determined with a coordinate measuring machine (Prismo Vast 5 HTG, Zeiss), with an accuracy of 1/100 mm. The

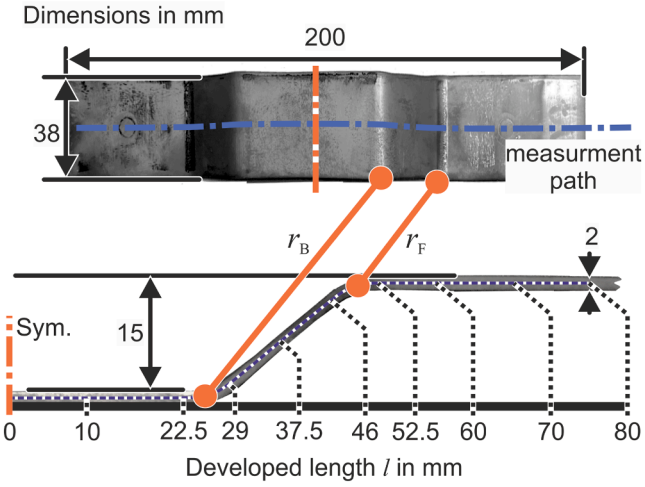

Fig. 9. Formed hat-shaped part with dimensions. Assignment of the developed length l to characteristic positions of the stretch formed hat-shaped part with an average radius at the bottom r_B and at the flange r_F of 8.5 mm.

top and bottom of the formed hat-shaped specimens are traced with a probe along the measurement path given in Fig. 9 and the measured coordinates are recorded at intervals of 0.1 mm. From the coordinates, curves are derived which describe the surface of the lower and upper side of the specimen. Those two curves are then used to calculate the sheet thickness s and thinning Δs. To compensate for fluctuations in the sheet thickness of the used material when calculating the sheet thinning Δs, the latter is calculated with respect to the initial sheet thickness of each individual sheet strip. The sheet thickness and thinning values are then assigned to an assumed centerline, which runs along half the sheet thickness. In this work, the sheet thinning Δs is compared along the developed length l of this assumed centerline.

5. Control-oriented modelling of thinning

The closed-loop control of the thinning distribution during the process, as described in Section 2, necessitates the quick calculation of the strain distribution within the soft sensor. This calculation is crucial for inferring the current thickness and for establishing a virtual process model that can be utilized by the process control. To minimize blind times and to enable fast control within the process stages, the calculation of the stretch forming operation must be performed within a timespan equal or shorter than a single press stroke. With a target stroke rate of up to 12 strokes/min, this results in a permitted maximum computation time of less than 5 s. This requirement of short calculation times prevents the use of full-scale FE simulations within the control loop. In principle, data-driven approaches can be chosen for this, wherein a database is generated by conducting parametrized FE simulations of the stretch forming stage and which is then utilized to train an artificial neural network or to create a simple lookup table, enabling the prediction of the thinning distribution. However, data-driven approaches are inflexible in case of a change in boundary conditions (e.g., geometry of the tools, material behavior, friction) and usually do not allow for a robust extrapolation. Therefore, a semi-analytical element-based model is developed that allows short run times by using simplifying assumptions and the temperature estimation as a model input, while at the same time allowing for an easy applicability to other problems.

In the next section, the underlying methodology and physics of the model are described together with the assumptions (Section 6.1). Subsequently, the individual steps of the computation procedure with details for the implementation are developed step by step (Section 6.2).

5.1. Model physics and assumptions

An element-based time-discrete approach is the basis of the model. The plastic deformation of the elements during stretch forming is calculated by solving for force equilibria, linearized element stiffness and the theory of plasticity. The combination of these methods into a novel, predominantly closed-form solution enables the sufficiently fast computation of a complex thermo-mechanical stretch forming process. Fig. 10 summarizes the fundamental concept of the model and it is detailed in the following.

Initially, the sheet is divided into elements of equal size. Since the process is symmetrical, with the appropriate symmetry conditions, the discretization and calculation of half of the component is sufficient. Therefore, half of the initial flat sheet within the tool having a length of $w_D + w_{BH} = 80$ mm (compare Fig. 5) is divided into 640 equal sized elements along the length - e.g., the neutral fiber - direction. This results in an initial element length $l_{ELE,t0}$ of 0.125 mm, allowing the final bending radii to be discretized with about 50 elements. Besides, an element width w_{ELE} corresponding to the sheet width in the experiments of 38 mm is assigned to each element. To account for the strain distribution over the sheet thickness resulting from bending loads in the tool radii areas, the elements in those regions are further subdivided into 20 segments in the sheet's thickness direction. With an initial sheet thickness of 2 mm this subdivision yields an initial segment height $h_{SEG,t0}$ of

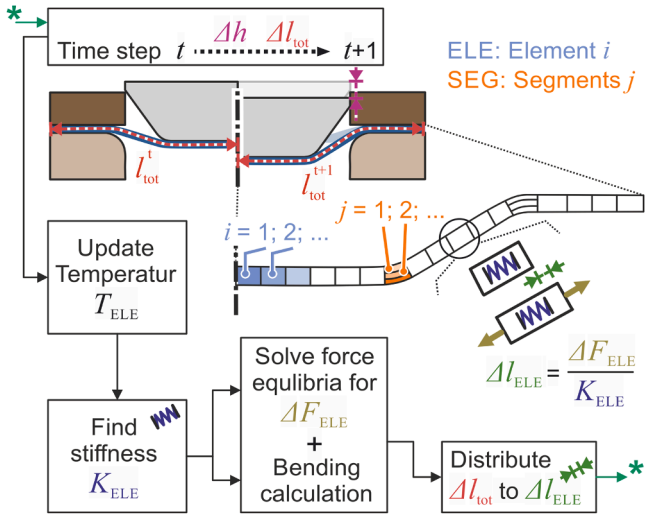

Fig. 10. Concept of the model. Fundamental concept and procedure for the quick computation of hot stretch forming.

0.1 mm, which was found to be a sufficiently accurate resolution for the closed-loop control. Since the elements are only segmented along the thickness direction, the segment width is equal to the element width. Due to the assumption of symmetry, the model in its presented form is not applicable to processes in which the sheet material slides over the center of the punch during forming.

The sheet width w is several times the sheet thickness s (here $w = 19 \times s$). Therefore, it is assumed that the plastic strains in the width direction are approximately equal to zero and plastic strains occur only in the length and thickness direction, so that the plane strain condition holds for an analysis of the problem viewed from the side (c.f. Fig. 10). A calculation of the sheet metal thinning with the model for the forming of sheet metal strips, where $w = s$, is therefore not valid, as more complex strain distributions than the ones assumed may occur. The material is modelled as isotropic, which includes isotropic hardening. Thus, the flow stress remains constant for load reversal. The interaction between plasticity and temperature in the component is neglected. Hence, the thermal and mechanical computations are decoupled. In this work, the temperature distribution in the sheet is derived directly from the measurements of a thermal imaging camera, and is used as input to the mechanical model. In future work, as described in Section 2, an external algorithm, which is not part of the presented model, shall be used to compute the temperature distribution.

The elements are assigned a new temperature T_{ELE} (from the thermal camera) within the calculation depending on their position in each time step. Likewise, the tool position is given as a function of time and is thus known for each time step. Based on the known tool position, with the assumption that the overall shape of the workpiece is determined by the tool ("shape constrained"), the total elongation of the central sheet fiber l_{tot} at each time step can be derived from the updated sheet geometry (Section 6.2.1). The assumption is justified as the tensile stresses resulting from the stretching process counteract bending-induced rounding of the bottom and wall areas. Furthermore, it is assumed that there is no straightening of already bent sheet areas at the tool radii. Accordingly, the modeling is not applicable to deep-drawing processes, which have a significant sheet draw-in resulting in bending of the side walls and in re-straightening of bent areas.

The total elongation l_{tot} is distributed by the model to the individual sheet elements and thus a local strain distribution is calculated, respectively updated, time-step by time-step. To derive this distribution, each element is first assigned a linearized stiffness K_{ELE} valid for the time step on the basis of the current, local temperature- and strain-rate-dependent yield curves. Taking into account the frictional forces in

the die, the equilibrium of forces is then formulated and solved for each element. On the basis of these element forces F_{ELE}, the stresses in the elements are calculated and, finally, the element elongation l_{ELE} is calculated by means of the element stiffness (Section 6.2.5).

In stretch forming, there is also a bending of the sheet in the region of the tool radii. Therefore, the stress and strain distribution resulting from the bending must be taken into account for the elements in these areas (Section 6.2.3). The actual bending radius and angle in each time-step are predetermined by the geometry when assuming the aforementioned constrained shape. In analogy to the Euler-Bernoulli hypothesis, plane cross sections are assumed to remain plane and perpendicular to the surface. Therefore, the through-thickness strain distribution is always linear. Based on the findings of Zhang et al. (2007), the shear force components and shear stresses are neglected. Therefore, from the normal forces acting on the bent elements – resulting from the stretch forming – and with the assumption of linear strain distribution, the distribution of stress in the bent elements can be derived.

5.2. Implementation of the computational procedure

The continuous forming process is divided into discrete time steps with a duration Δt. In each time step, the implemented calculation procedure shown in Fig. 11 is executed, which will be explained in the following. The choice of the time step duration Δt depends on the total time span t_{tot} – duration from initial sheet contact to the end of the stretch forming – which in turn is a function of the stroke rate f_{SR} and the drawing depth h. For the developed algorithm, convergence and stability is achieved if

$$\Delta t \leq (1\text{mm} \bullet t_{tot}/(2 \bullet h[\text{mm}]) \tag{2}$$

The latter criteria was identified empirically within the scope of the computational validation. It is intended solely as a guideline and does not provide a minimization of the time step duration.

5.2.1. Determination of the target geometry

In the first step of each time increment, the current workpiece geometry is calculated based on the punch displacement, i.e., the drawing depth $h(t)$. With the assumptions that the bends are introduced locally at the radius of the die as well as the punch and that the bottom, wall and flange remain flat during forming the total stretched length $l_{tot}(h)$ of the center fiber of one workpiece half can be determined:

$$l_{tot} = l_b + l_w + l_f + 2 \cdot l_r \tag{3}$$

$$\text{with} l_w = \frac{l_{w,0} - 2 \cdot \left(r_T + \frac{s}{2}\right) \cdot \sin(\theta(h))}{\cos(\theta(h))} \tag{4}$$

$$\text{and} l_r = \theta(h) \cdot \frac{\pi}{180} \cdot \left(r_T + \frac{s}{2}\right) \tag{5}$$

The angle θ is a function of the drawing depth h which will not be further specified here. For the variables used in Eqs. (3)-(5) a graphical explanation is given in Fig. 12. With the total stretched length $l_{tot}(h)$ the strain applied within the time span of the time increment Δt can be derived. The segmentation of the strain, i.e. the total length change, to the individual elements is carried out later in calculation step 5.

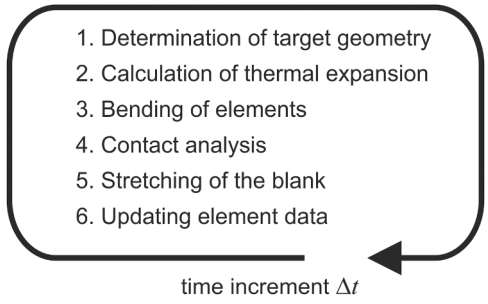

Fig. 11. Steps of the implemented model. Computation sequence for a discrete time step of the implemented process model.

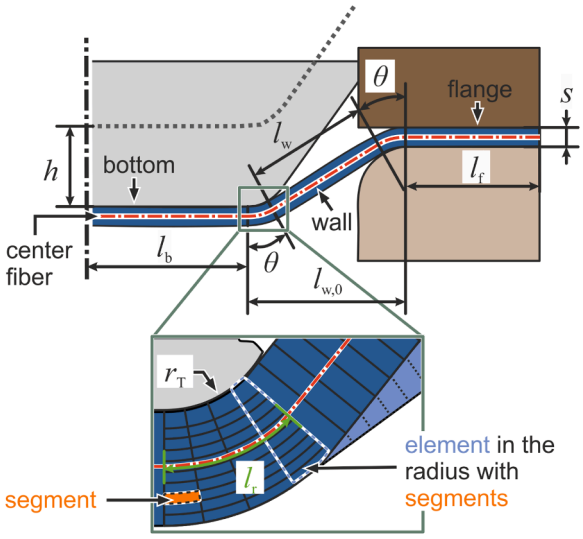

Fig. 12. Subdivision of the length of the center fiber. Length of the center fiber of the workpiece and close-up of the punch radius with the division of the sheet into elements and segments.

5.2.2. Update of element temperature and calculation of the thermal expansion

After determining the current geometry (Section 6.2.1), a temperature is assigned to each of the elements based on their previously calculated positions. The temperature data is an input for the model provided by the upstream sensors. For the future application of the model, the temperature is to be provided by a temperature soft sensor (Martschin et al., 2023). For the development of the current model, this input is gathered from thermal imaging camera data. With a frame rate of the thermal imaging camera of 80 Hz, 12 thermal images - i.e., data sets for the temperature distribution at specific timings - are available as input at a stroke rate f_{SR} of 35/min and 32 images at a f_{SR} of 10/min per stretch forming cycle. Since the timing of the individual loop passes of the stretch forming model does not coincide with the recording timing of the thermal imaging camera, interpolation is performed between the individual data sets (thermal images) within the model. Hereby, the temperature distribution is approximated for each calculation loop pass.

From the temperature difference obtained for each time increment - i.e., between two loop passes -, the thermal expansion for the individual elements is calculated. The thermal expansion coefficients from Spittel and Spittel (2009) are used. The strains induced by the thermal expansion are superposed to the strains from the previous calculation loop. In the first loop cycle, these expansions are initially set to zero.

5.2.3. Bending of elements

It is assumed that the bending in the radii and stretching of the whole sheet can be considered sequentially within the control-oriented calculation model, since the strains in each time step are small due to the large number of steps. First, the bending of the outer elements of the wall is calculated, starting with those closest to the bottom respectively the flange. The elements are bent until the sum of all individual element angles θ_{ELE} (Fig. 13) in each bending radius equals the current total bending angle θ. The sheet draw-in from the area under the blank holder must be smaller in each step than the change in the arc length of the bend, as otherwise elements at the boundary to the wall area would have to be straightened again in order not to exceed the total bending angle. This condition is not met in deep drawing, so that the calculation

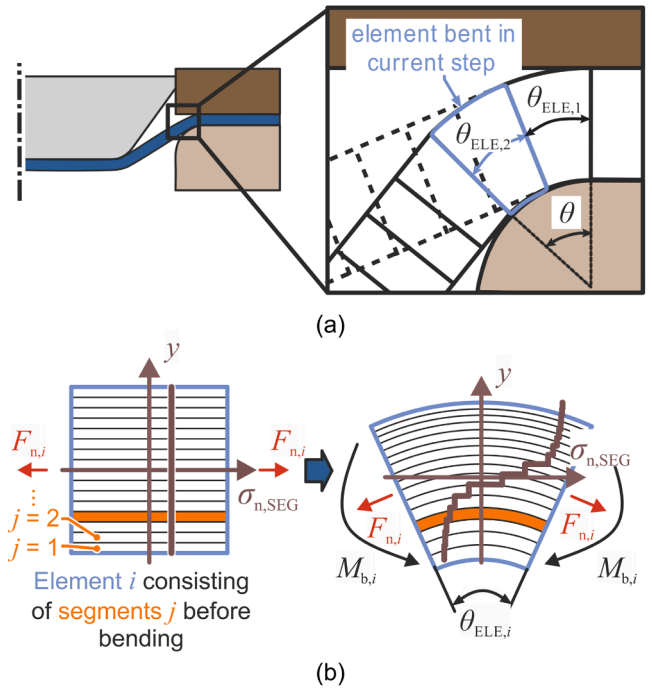

Fig. 13. Bent elements with segmentation. (a) Bent elements at the tool radius. (b) Normal stress $\sigma_{n,SEG}$ in the segments j of the element i loaded with the normal force $F_{n,i}$ before and after bending to the element angle $\theta_{ELE,i}$.

method presented can only be used for stretch bending with low sheet draw-in.

The inner radius of the bend is given by the radius of the tool r_T. The element angle and hence the average element length is dependent on the normal force $F_{n,i}$ acting on the element i induced from the stretching. Within the calculation loop, the normal force acting on each element from the previous loop pass is used to calculate the bending stresses and strains in the segments j. The only exception is the very first calculation cycle where no tensile stresses occur. Within a segment, strain and stress are considered constant due to the small segment height. Therefore, the sum of the segment normal stresses $\sigma_{n,SEG}$ of the number of segments N_{SEG} weighted by the segment height h_{SEG} and element width w_{ELE} must be equal to the normal force.

$$F_{n,i} = \sum_{j=1}^{N_{SEG}} \sigma_{n,SEG,j} \cdot h_{SEG,j} \cdot w_{ELE} \tag{6}$$

Assuming that plane cross sections remain plane, the resulting strain from the bending with the moment $M_{b,i}$ is distributed linearly across the sheet thickness. However, since the stress is non-linearly related to the strain, the superimposed tensile stress does not cause a homogeneous increase of the final bending stress. Instead, the element angle, and thus the strain, adjusts so that Eq. (6) holds. For this reason, an iterative determination of each element angle and the length of the neutral fiber in the element is necessary. The numerical determination of the bending angle starts by assuming upper and lower limit values. For each of these values, the bending stresses are calculated and the resulting mean stress is compared with the stress before bending. Using the interval bisection method, the limit values are adjusted until the deviation between mean stress and the stress before bending becomes sufficiently small.

5.2.4. Contact analysis

After the bending of the elements is finished and the sum of the element angles equals the current predefined bending angle θ, the contact situation is analyzed. Based on their position, the elements are assigned to the different areas of the workpiece. It is assumed that the force transmission between tools and sheet is localized at the areas of the

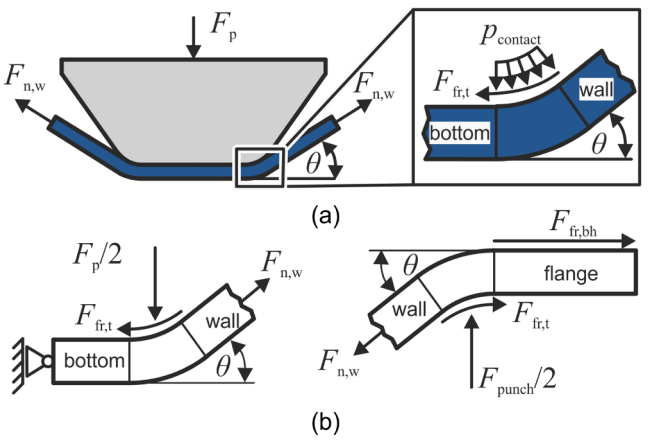

Fig. 14. Forces acting on the punch and sheet. (a) Punch force F_p and normal force in the wall $F_{n,w}$ as well as resulting friction force $F_{fr,t}$ due to the contact pressure of the punch $p_{contact}$. (b) Section view of the lower and upper half of the component.

radii (Fig. 14). Here the contact pressure between the sheet and the die is assumed to be equally distributed on the contact surface which means that the same frictional force acts on all elements in the area.

The total friction forces at the radii can be calculated according to:

$$F_{fr,t} = \frac{1}{2} \cdot \mu \cdot F_p \cdot \cos\frac{\theta}{2} \tag{7}$$

By means of a global force equilibrium (Fig. X), the punch force is given with:

$$F_p = 2 \cdot F_{n,wall} \cdot \sin\theta \tag{8}$$

The friction force between the blank holder and the flange can furthermore be determined via the ram position, since the blank holder force can be calculated as a function of the punch position using the stiffness of the blank holder springs.

5.2.5. Stretching of the blank

The main part of the calculation loop is the stretching step. Based on the geometry of the sheet, the change in total length in the current step can be determined. This change in length must then be distributed between the elements to satisfy the following equilibrium condition for each element i:

$$F_{n,i} = F_{n,w} \cdot \cos\delta_i - X_i \cdot F_{fr,t} - Y_i \cdot F_{fr,bh} \tag{9}$$

Where δ_i is the sum of the element angles from the wall section to element i. X_i and Y_i describe the proportions of the total frictional forces from the tool $F_{fr,t}$ and the blank holder $F_{fr,bh}$ that occur up to element i, respectively. X increases linearly with the angle δ_i between element i and the wall.

By dividing the process into short time steps and thus small changes of the strain, the stress-strain behavior within a single step can be considered linear. Thus, the stiffness of an element K_i within a time step can also be assumed to be linear. This element stiffness K_i is calculated with an incrementally imposed length change $\Delta l_{incr,i}$ and the resulting change in normal force $\Delta F_{incr,i}$. Here, Δl_{incr} does not represent the final element length change within an entire time step Δt, instead it is solely an incremental test value for the linearization at the beginning of each time step. Hence, ΔF_{incr} does not represent the total force change within a time step.

$$K_i = \frac{\Delta F_{incr,i}}{\Delta l_{incr,i}} \tag{10}$$

The incremental length change of the element Δl_{incr} must be close to the value of the expected length change of the time step. With this the

incrementally imposed logarithmic strain and strain rate follows:

$$\varphi_{\mathrm{incr}} = \frac{2}{\sqrt{3}} \cdot \ln\left(\frac{l + \Delta l_{\mathrm{incr}}}{l_0}\right) \tag{11}$$

$$\dot{\varphi}_{\mathrm{incr}} = \frac{\varphi_{\mathrm{incr}}}{\Delta t} \tag{12}$$

Using the logarithmic strain φ_{incr}, the strain rate $\dot{\varphi}_{\mathrm{incr}}$ and the temperature T, the incremental normal stress σ_{incr} is determined utilizing the material model, i.e. the flow curve extrapolation (see Eq. (1)). On this basis, the incremental difference in normal force $\Delta F_{\mathrm{incr},i}$ for each element can be described by Eq. (13). Here, w_{ELE} is the constant element width, $s_{\mathrm{incr},i}$ is the sheet thickness resulting from the strain φ_{incr} and σ_{n}^{t} as well as s^{t} are the start values for the normal stress and sheet thickness at the time t. Additionally, to distinguish between the elastic and plastic regions, specific cases are considered. By substituting Eq. (13) into Eq. (10), the resulting stiffness is given by Eq. (14).

$$\Delta \mathrm{F}_{\mathrm{incr,i}} = \left[\sigma_{\mathrm{n,incr},i}(\varphi_{\mathrm{incr},i}, \dot{\varphi}_{\mathrm{incr},i}, T_i) \cdot s_{\mathrm{incr},i}(\varphi_{\mathrm{incr},i}) - \sigma_{\mathrm{n},i}^{t} \cdot s_i^{t}\right] \cdot w_{\mathrm{ELE}} \tag{13}$$

$$\mathrm{K}_i = \frac{\left[\sigma_{\mathrm{n,incr},i}(\varphi_{\mathrm{incr},i}, \dot{\varphi}_{\mathrm{incr},i}, T_i) \cdot s_{\mathrm{incr},i}(\varphi_{\mathrm{incr},i}) - \sigma_{\mathrm{n},i}^{t} \cdot s_i^{t}\right] \cdot w_{\mathrm{ELE}}}{\Delta l_{\mathrm{incr},i}} \tag{14}$$

For the curved elements, the inhomogeneous stress distribution over the sheet thickness and the boundary condition of constant inner radius must be considered. Therefore, the stiffness of each segment j within an element is calculated separately. The element stiffness of the bent elements is then determined as the sum of the segment stiffness. Using the linear element stiffness, the distribution of the elongation can be determined by considering the workpiece as a system of springs connected in series. However, the influence of the frictional force and the angular difference of the bottom area and flange to the wall must still be taken into account. The change of the length of the workpiece is then given by the sum of the changes of the length of all elements. This expression can be represented as the sum of the quotients of nominal force and the element stiffness.

$$\Delta l_{\mathrm{tot}} = \sum_{i=1}^{N_{\mathrm{ELE}}} \Delta l_{\mathrm{i}} = \sum_{i=1}^{N_{\mathrm{ELE}}} \frac{\Delta F_i}{K_i} \tag{15}$$

The difference in normal force of the elements between two subsequent time steps is obtained using Eq. (9).

$$\Delta F_{\mathrm{i}} = F_{\mathrm{n},i}^{t+1} - F_{\mathrm{n},i}^{t} = F_{\mathrm{n,w}}^{t+1} \cdot \cos\left(\delta_i^{t+1}\right) - F_{\mathrm{n,w}}^{t} \cdot \cos\left(\delta_i^{t}\right)$$

$$+ X_i^{t+1} \cdot F_{\mathrm{fr,t}}^{t+1} - X_i^{t} \cdot F_{\mathrm{fr,t}}^{t} + Y_i^{t+1} \cdot F_{\mathrm{fr,bh}}^{t+1} - Y_i^{t} \cdot F_{\mathrm{fr,bh}}^{t} \tag{16}$$

The maximum normal force is present in the wall area of the component. By substituting Eqs. (14) and (16) into Eq. (15) and rearranging, the maximum normal force at the new time $t+1$ can be determined as a function of the sheet length change Δl_{tot} and the stiffness of all elements K_i:

$$F_{\mathrm{n,w}}^{t+1} = \frac{\Delta l_{\mathrm{tot}} + \sum_{i=1}^{n_{\mathrm{ELE}}} \frac{F_{\mathrm{n,w}}^{t} \cdot \cos\left(\delta_i^{t}\right) + X_i^{t+1} \cdot F_{\mathrm{fr,t}}^{t+1} - X_i^{t} \cdot F_{\mathrm{fr,t}}^{t} + Y_i^{t+1} \cdot F_{\mathrm{fr,bh}}^{t+1} - Y_i^{t} \cdot F_{\mathrm{fr,bh}}^{t}}{K_i}}{\sum_{i=1}^{N_{\mathrm{ELE}}} \frac{\cos\left(\delta_i^{t+1}\right)}{K_i}} \tag{17}$$

The normal forces in the other component areas can then be computed using Eq. (9). The difference between the element normal force and the previous calculation step is used to obtain the element length change:

$$\Delta l_i = \frac{\Delta F_i}{K_i} \tag{18}$$

Now, with Eq. (18) the actual length change of each element Δl_i (not the incremental length change) can be inferred. Based on this, the incremental strain and stress can be updated to account for the whole current time step.

5.2.6. Implementation details

The model presented above is implemented in Matlab R2022b on a computer with an Intel Core i7 7th Gen processor (CPU @ 2.8 GHz, 4 cores), 16 GB RAM and Windows 10 operating system. A runtime of about 4 s for each of the examples of stretch forming process configurations shown below is achieved.

6. Validation of the model

The following sections assess the validity and prediction quality of the model developed above through a comparison between the model's output and the experimental results obtained using the setup presented in Section 4.1. First, the prediction of sheet thinning during stretch drawing after heating to $T_\gamma = 1100\,^{\circ}\mathrm{C}$ without further active pre-cooling at different stroke rates f_{SR}, i.e. different punch speed profiles over time (see Fig. 7), is analyzed. Subsequently, the model prediction of the effect of different pre-cooling setups at a constant stroke rate is examined. A constant coefficient of friction μ of 0.3 is assumed for all calculations with the control-oriented model.

6.1. Influence of stroke rate without active pre-cooling

In Figs. 14 and 15 and, the temperature distribution before $T(t_{\varepsilon,\mathrm{start}})$ and after forming $T(t_{\varepsilon,\mathrm{end}})$, as well as the measured (Exp.) and modeled (Mod.) sheet thinning Δs at 10 and 35 strokes per minute are given. Depending on the stroke rate, different temperature distributions are present, particularly in the area of the punch ($0 < l < 22.5$) and blank holder ($52.5 < l < 80$) at the start of forming $t_{\varepsilon,\mathrm{start}}$, which result from

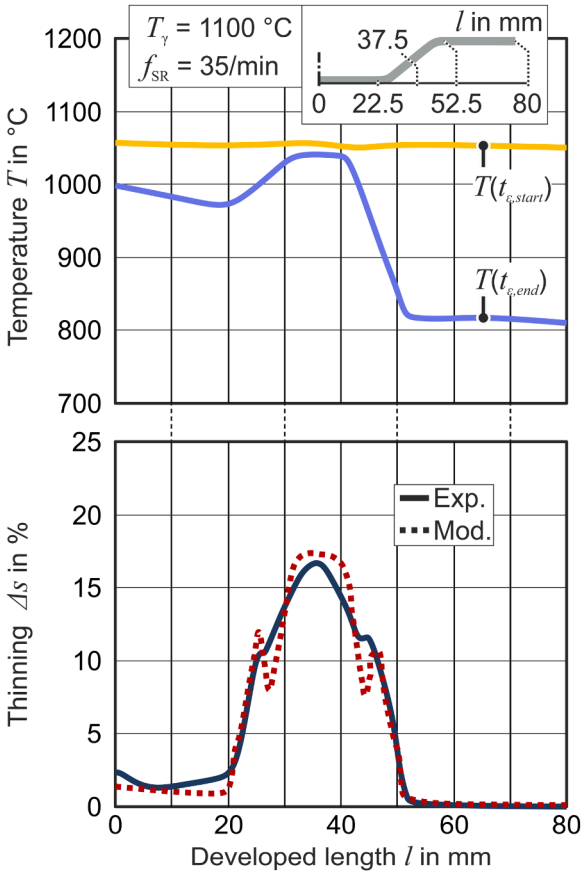

Fig. 15. Temperature and thinning distribution with a stroke rate f_{SR} = 35/min. Comparison of the thinning of the formed hat-shaped part calculated with the model (Mod.) and the thinning measured in the experiments (Exp.).

different timespans for a heat exchange. With a stroke rate $f_{SR} = 35$/min, the initial temperature distribution before forming is almost homogeneous (~ 1050 °C), hence this process setting serves as a reference in the following. Here, with the experimental setup a nearly symmetrical thinning profile is obtained with respect to the center of the side wall (l = 37.5), with a maximum thinning Δs of 16.7%. The overall thinning profile of the Exp. is accurately approximated by the control-oriented modeling. However, the model overestimates the maximum thinning value at the center of the side wall by 0.7% and predicts, based on the temperature input data, a 5.4 mm wide plateau for the maximum thinning, which is not present in the experiment. The latter could be attributed to an overestimation of the influence of strain hardening with an increase in the strain rate. Additionally, the model predicts a localization of thinning in the radii, with deviations between Exp. and Mod. of up to 3.7%, which also does not occur in the experiments.

At a lower stroke rate of f_{SR} = 10/min, prior to forming the temperature in the sheet drops to 942 °C in the area of the flange and to as low as 1015 °C in the area of the bending radii. In the Exp., this facilitates a localized thinning (up to 21%) in the side wall and a reduced material flow from the area of the flange, whereby the maximum thinning is shifted from the center of the side wall to the left. The maximum thinning Δs_{max} (deviation Exp. and Mod. for Δs_{max} 0.4%) and its offset are also reproduced by the model. However, as before, the model predicts an additional localization in the area of the radii, which does not occur in the experiment. Apart from that, the thinning of the components bottom is underestimated. Overall, the results show that the model is able to reproduce the influence of different stroke rates, which is affecting the time-temperature distribution and the strain rate, on the thinning distribution.

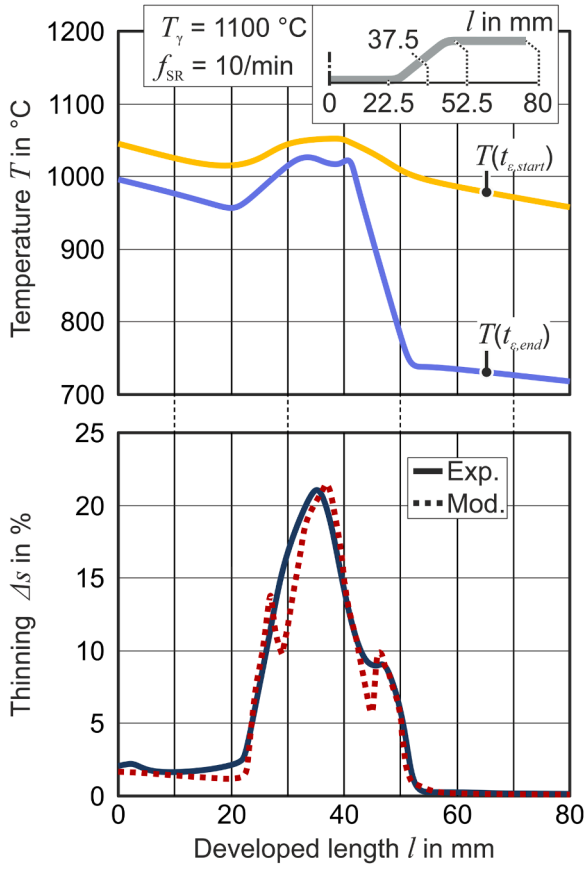

Fig. 16. Temperature and thinning distribution with a stroke rate f_{SR} = 10/min. Comparison of the thinning of the formed hat-shaped part calculated with the model (Mod.) and the thinning measured in the experiments (Exp.).

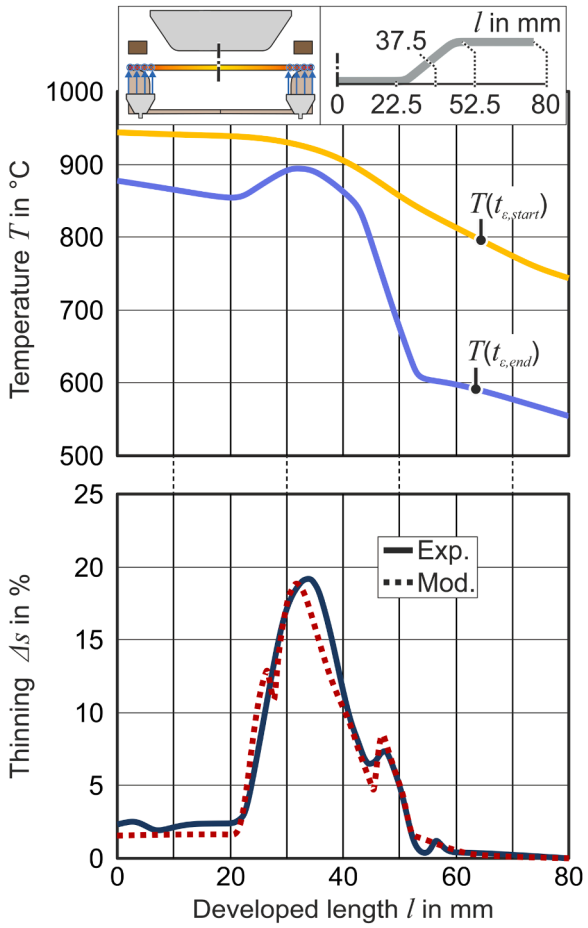

Fig. 17. Temperature and thinning distribution with cooling nozzle configuration 2. Comparison of the thinning of the formed hat-shaped part calculated with the model (Mod.) and the thinning measured in the experiments (Exp.) with pre-cooling at position l = 55 mm with an austenitization temperature T_γ = 1100 °C and a stroke rate f_{SR} = 10/min.

6.2. Variation of the pre-cooling setup

After reviewing that the influence of the stroke rate can be reproduced by the model, the analysis will now focus on reproducing the effect of different initial temperature distributions set by pre-cooling at a constant stroke rate of f_{SR} = 10/min on thinning. After pre-cooling of the flange (configuration 2), the temperature in the outer area of the flange (l = 80.0) is 745 °C, increases roughly linearly up to the middle of the side wall, and reaches 950 °C at the center of the bottom (l = 80.0). In the time span of the forming operation, especially the temperature in the area of the flange drops considerably (Δt_{max} = 188 °C), while the temperature in the area of the side wall decreases minimally (Δt_{max} = 67 °C) due to the lack of contact between the sheet and the tools. This enhances the flow of material in the area of the frame, which is oriented towards the parts bottom, so that a maximum thinning Δs_{max} of 19.2% occurs here during the experiment. The model is qualitatively reproducing the result of the experiment with configuration 2. The model predicts the position of the thinning maximum 2.1 mm further to the left and the deviation between the maximum thinning Δs_{max} in Exp. and Mod. is 0.4%. In addition, the model indicates a local strain peak in the area of the radius adjacent to the bottom of the component, which does not occur in the experiment. However, the strain peak in the radius adjacent to the flange is well determined by the model.

When adapting the pre-cooling of configuration 3, the bottom of the component in particular is cooled. The temperature before forming in the area of $0 < l < 20$ is about 800 °C and increases to about 920 °C in the

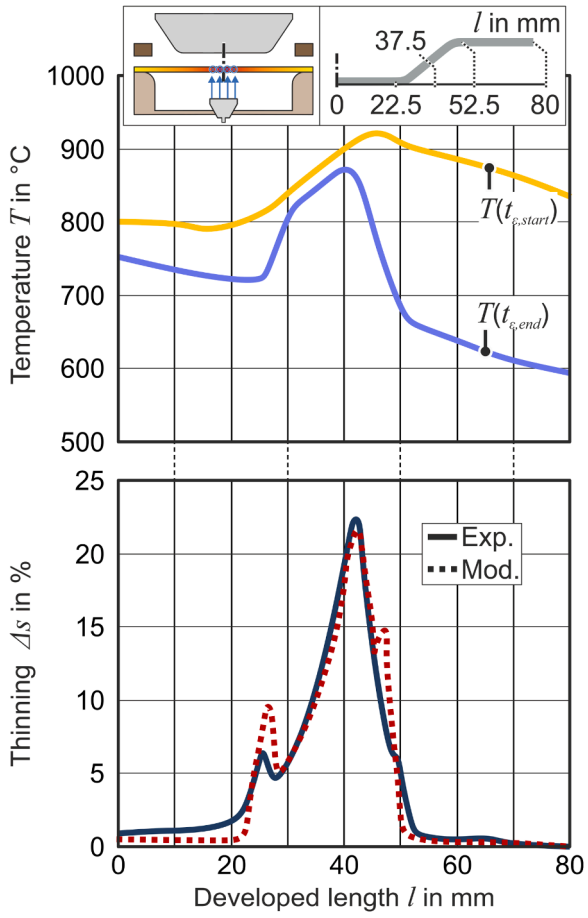

Fig. 18. Temperature and thinning distribution with cooling nozzle configuration 3. Comparison of the thinning of the formed hat-shaped part calculated with the model (Mod.) and the thinning measured in the experiments (Exp.) with pre-cooling at position $l = 0$ mm with an austenitization temperature $T_\gamma = 1100$ °C and a stroke rate $f_{SR} = 10$/min.

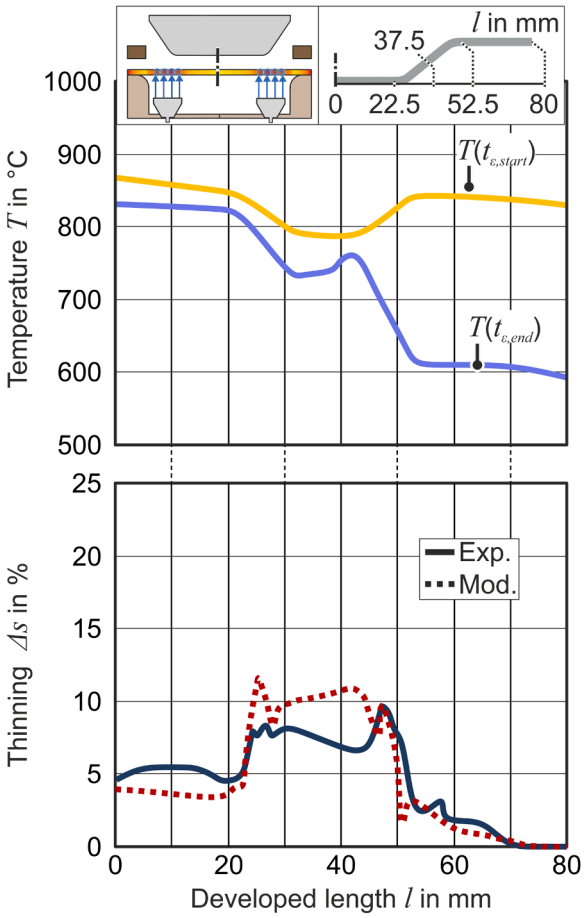

Fig. 19. Temperature and thinning distribution with cooling nozzle configuration 4. Comparison of the thinning of the formed hat-shaped part calculated with the model (Mod.) and the thinning measured in the experiments (Exp.) with pre-cooling at position $l = 35$ mm with an austenitization temperature $T_\gamma = 1100$ °C and a stroke rate $f_{SR} = 10$/min.

radius adjacent to the flange and decreases again to the outer area in the flange. This amplifies thinning in the area of the wall adjacent to the flange ($37.5 < l < 52.5$). Here, in the experiment, a maximum thinning Δs_{max} of 22.4% is observed. In the radii of the heat shaped profile, local strain peaks with a thinning of about 6.5% are obtained. The model prediction matches the shape of the thinning profile from the experiments and the maximum value in the area of the side wall well (deviation at Δs_{max} of 0.8%). However, there are deviations between Mod. and Exp. of up to 6.3% in the radii and also in the area of the bottom, which merges into the radius ($l = 20$), of up to 2%. Accordingly, the localization of the strain at the bending radii was overestimated by the model also in this configuration. As a consequence, the material flow from the thickness in the area of the bottom into the side wall is also not perfectly approximated.

In the previously considered configurations, pre-cooling promoted a material flow out of the side wall. However, with config. 4, the temperature in the area of the side wall is lowered before forming so that it is ~50 °C below the temperature of the adjacent radii. Therefore, increasing locally the yield stress within the side wall area. In the experiment, this results in material thinning Δs in the area of the bottom of up to 5.4% and in the flange of up to 3.1%. The thinning in the side wall, especially when considering the previously analyzed configurations, is only slightly larger with an average Δs of ~7.6%. In the experiment with config. 4, the maximum thinning value is set at the bending radius adjacent to the flange with an Δs of 9.5%. The model also predicts a comparatively low thinning in the frame, which, however, is on average 2.3% higher than the experimentally determined values. In addition, the thinning in the bottom of the hat-shaped profile is underestimated on average by an Δs of 1.4%. As in the previous example (config. 3), underestimating the thinning in the components bottom by the model causes an overestimation of the strain peak in the radius adjacent to it.

The weaknesses of the developed quick control-oriented model approach thus include reproducing the material flow over the radii from the bottom as well as from the flange into the sidewall. The more the material has to flow over the radius, the less accurate the model becomes. Therefore, as postulated under the assumptions in Section 6.1, the model is not suitable for processes with significant sheet draw-in, such as deep drawing. However, the examples presented prove that for the stretch forming under consideration the overall shape of the thinning distribution, which is ultimately the most relevant factor for the process control, as well as the estimation of the maximum thinning value, can be predicted well by the model.

7. Conclusions

As a first step towards controlling the thinning distribution in stretch forming, e.g. during multi-stage press hardening, a control-orientated prediction model was developed enabling feedback of the thinning distribution within the process and serving as model basis for control. Unique to this new element-based model is the consideration of the spatially as well as time-variant temperature distribution within in blank

in the stretch forming stage. The latter temperature distribution has to be provided by sensors (e.g. thermal imaging camera) or a temperature soft sensors. To validate the model, the predicted values were compared with those from a setup for simulating the multi-stage process under consideration.

- The quick model can compute the thinning distribution of the stretch formed hat-shaped profiles within a time span of 4 s, when the temperature distribution over time is given and is hence qualified for process control. Therefore, for stroke rates up to 12/min, an update of the current thinning distribution can be fed back within the duration of a process stage.
- The model can reproduce both the influence of different stroke rates on the final thinning distribution, which exerts a variation in strain rate and temperature-time distributions, as well as the influence of different pre-cooling scenarios. The assumption within the model that the thermal calculation can be decoupled from the mechanical calculation is therefore justified.
- The general shape of the thinning distribution and especially the region of maximum thinning is predicted accurately by the model. However, the thinning in the radii is usually overestimated. A weak representation of the material flow over the radii reduces the model accuracy in the area of the radii.
- With the experimental setup, it was demonstrated that the thinning of hat-shaped parts can be selectively set by using actuators such as a heating system and cooling nozzles within the multi-stage hot sheet metal forming process.

8. Outlook

Two main aspects need to be addressed in the context of further developments, which are model improvement as well model utilization. In particular, the computing time of the model must be further reduced so that the model can also be used for stroke rates greater than 12/min. A promising approach seems to be to employ a faster numerical method than the interval bisection method to determine the bending angle within the proposed model. In addition, implementing the model using a programming language such as Python could save computing time. Due to the assumption of a small sheet draw-in and that the side walls of the hat-shaped profile remain flat, the modeling is not directly applicable to the more common forming process deep drawing. It must be investigated whether transferability is possible by implementing a curvature calculation for the side walls combined with an extended draw-in computation. Furthermore, it is important to examine how the process control should adapt the control variables of the multi-stage process on the basis of the output of the presented new model. One approach could be to define an optimization problem that compares the model prediction with a target distribution and then adjusts the control variables on the basis of a fast reduced system model.

CRediT authorship contribution statement

Philipp Rethmann: Writing – review & editing, Visualization, Software, Investigation, Formal analysis. **Juri Martschin:** Writing – review & editing, Writing – original draft, Visualization, Validation, Software, Methodology, Investigation, Formal analysis, Data curation, Conceptualization. **Malte Wrobel:** Writing – review & editing. **Joshua Grodotzki:** Writing – review & editing, Software, Formal analysis, Conceptualization. **A. Erman Tekkaya:** Writing – review & editing, Supervision, Project administration, Funding acquisition, Conceptualization. **Thomas Meurer:** Writing – review & editing.

Declaration of Competing Interest

The authors declare that they have no known competing financial interests or personal relationships that could have appeared to influence the work reported in this paper.

Acknowledgments

The authors thank the German Research Foundation (DFG) for the financial support of project 424334660 in the Collaborative Research Centre SPP2183 “Property-controlled forming processes” (German: Eigenschaftsgeregelte Umformprozesse). Furthermore, great appreciation is extended to Tom Adams for conducting the tensile tests and fitting of the flow curve models.

References

Attar, H.R., Zhou, H., Li, N., 2021. Deformation and thinning field prediction for HFQ® formed panel components using convolutional neural networks. IOP Conf. Ser.: Mater. Sci. Eng. vol. 1157, 12079. https://doi.org/10.1088/1757-899X/1157/1/012079.

Behrens, B.-A., Hübner, S., Sunderkötter, C., Gebel, L., Gnaß, S., Berndt, G., Trimborn, C., Pfeffer, C., 2018. Influence of process parameters on the hot stamping of carbon-martensitic chromium steel sheets. IOP Conf. Ser.: Mater. Sci. Eng. vol. 418, 12007. https://doi.org/10.1088/1757-899X/418/1/012007.

Belanger, P., Lage, M.L., Ruiz, L.R., Isaksson, K., 2017. New Zn multistep hot stamping innovation. Proc. 6th Int. Conf. Hot Steel Met. Form. High. -Perform. Steel 327–335.

Brosius, A., Karbasian, H., Tekkaya, A.E., Lechler, J., Merklein, M., Geiger, M., Springer, R., Schaper, M., Bach, F.W., Hoffmann, H., 2007. Modellierung und Simulation der Warmblechumformung: Aktueller Stand und zukünftiger Forschungsbedarf. In: Geiger, M., Merklein, M. (Eds.), Tagungsband 2. Erlanger Workshop Warmblechumformung. Erlangen,, pp. 37–58.

Cowper, G.R., Symonds, P.S., 1957. Strain-Hardening and Strain-Rate Effect in the Impact Loading of Cantilever Beams, Defense Technical Information Center, Fort Belvoir, VA.

Demazel, N., Laurent, H., Coër, J., Carin, M., Le Masson, P., Favero, J., Canivenc, R., Salmon-Legagneur, H., 2018. Investigation of the progressive hot die stamping of a complex boron steel part using numerical simulations and Gleeble tests. Int J. Adv. Manuf. Technol. vol. 99, 803–817. https://doi.org/10.1007/s00170-018-2532-6.

Dieck, S., Rosemann, P., Kromm, A., Halle, T., 2017. Reversed austenite for enhancing ductility of martensitic stainless steel. IOP Conf. Ser.: Mater. Sci. Eng. vol. 181, 12034. https://doi.org/10.1088/1757-899X/181/1/012034.

Hamamoto, S., Omori, H., Asai, T., Mizuta, N., Jimbo, N., Yamano, T., 2017. Steel sheets for highly productive hot stamping. Kobelco Technol. Rev. vol. 35, 39–44.

Kadlec, P., Gabrys, B., Strandt, S., 2009. Data-driven Soft Sensors in the process industry. Comput. Chem. Eng. vol. 33, 795–814. https://doi.org/10.1016/j.compchemeng.2008.12.012.

Kloeser, D., Martschin, J., Meurer, T., Tekkaya, E., 2021. Reduced order modelling for spatial-temporal temperature and property estimation in a multi-stage hot sheet metal forming process. Adv. Ind. Manuf. Eng. vol. 3, 100055 https://doi.org/10.1016/j.aime.2021.100055.

Löbbe, C., Hoppe, C., Becker, C., Tekkaya, A.E., 2015. Closed loop springback control in progressive die bending by induction heating. Int. J. Precis. Eng. Manuf. vol. 16, 2441–2449. https://doi.org/10.1007/s12541-015-0314-8.

Löbbe, C., Hering, O., Hiegemann, L., Tekkaya, A.E., 2016. Setting Mechanical Properties of High Strength Steels for Rapid Hot Forming Processes. Mater. (Basel, Switz.) vol. 9. https://doi.org/10.3390/ma9040229.

Lord, J.D., Morrell, R.M., 2010. Elastic modulus measurement—obtaining reliable data from the tensile test. Metrologia vol. 47, 41–49. https://doi.org/10.1088/0026-1394/47/2/S05.

Maeno, T., Mori, K., Nagai, T., 2014. Improvement in formability by control of temperature in hot stamping of ultra-high strength steel parts. CIRP Ann. vol. 63, 301–304. https://doi.org/10.1016/j.cirp.2014.03.005.

Martschin, J., Meya, R., Klöser, D., Meurer, T., Tekkaya, A.E., 2021. Control-Oriented Characterization of Product Properties during Hot Hole-Flanging of X46Cr13 Sheet Material in a Progressive-Die. Metals vol. 11, 349. https://doi.org/10.3390/met11020349.

Martschin, J., Wrobel, M., Grodotzki, J., Meurer, T., Tekkaya, A.E., 2023. Soft Sensors for Property-Controlled Multi-Stage Press Hardening of 22MnB5. Automot. Innov. vol. 6, 352–363. https://doi.org/10.1007/s42154-023-00238-z.

Mori, K., Maeno, T., Tsuchiya, M., Nanya, T., 2017. Inclusion of hot stamping operations in progressive-die plate forging of tailored high strength gear part. Int J. Adv. Manuf. Technol. vol. 90, 3585–3594. https://doi.org/10.1007/s00170-016-9705-y.

Nemat-Nasser, S., 2002. Experimentally-based Micromechanical Modeling of Metal Plasticity with Homogenization from Micro-to Macro-scale Properties. In: IUTAM Symposium on Micro- and Macrostructural Aspects of Thermoplasticity, vol. 62. Kluwer Academic Publishers, Dordrecht, pp. 101–113. https://doi.org/10.1007/0-306-46936-7_10. O.T.BruhnsE.Stein.

Ota, E., Yogo, Y., Iwata, T., Iwata, N., Ishida, K., Takeda, K., 2014. Formability Improvement Technique for Heated Sheet Metal Forming by Partial Cooling. KEM 622-623, 279–283. https://doi.org/10.4028/www.scientific.net/KEM.622-623.279.

Pérez Caro, L., Odenberger, E.-L., Schill, M., Niklasson, F., Åkerfeldt, P., Oldenburg, M., 2021. Springback prediction and validation in hot forming of a double-curved component in alloy 718. Int J. Mater. Form. vol. 14, 1355–1373. https://doi.org/10.1007/s12289-021-01615-x.

Spittel, M., Spittel, T., 2009. Steel symbol/number: X46Cr13/1.4034. In: Martienssen, W., Warlimont, H. (Eds.), Metal Forming Data of Ferrous Alloys - deformation behaviour, 2C1. Springer Berlin Heidelberg,, Berlin, Heidelberg, pp. 588–593. https://doi.org/10.1007/978-3-540-44760-3_89.

Suzuki, Y., Mori, K., Maeno, T., Sakakibara, K., Abe, Y., 2018. Improvement of formability using partial cooling during transfer in hot stamping of ultra-high strength steel parts. Procedia Manuf. vol. 15, 1119–1126. https://doi.org/10.1016/j.promfg.2018.07.379.

Tricarico, L., Palmieri, M.E., 2023. Robust Design of Deep Drawing Process through In-Line Feedback Control of the Draw-In. Appl. Sci. vol. 13, 1717. https://doi.org/10.3390/app13031717.

Zhang, D., Cui, Z., Ruan, X., Li, Y., 2007. An analytical model for predicting springback and side wall curl of sheet after U-bending. Comput. Mater. Sci. vol. 38, 707–715. https://doi.org/10.1016/j.commatsci.2006.05.001.